1 **Seasonal drivers of carbon cycle interannual variability**
2 **represented by the Community Earth System Model (CESM2)**
3

4 **W. R. Wieder[1,2*], Z. Butterfield[3], K. Lindsay[1], D. L. Lombardozzi[1], G. Keppel-Aleks[3]**

5

6 [1] Climate and Global Dynamics Laboratory, National Center for Atmospheric Research, Boulder,

7 CO 80307, USA.

8 [2] Institute of Arctic and Alpine Research, University of Colorado, Boulder, CO 80309, USA

9 [3] Department of Climate and Space Sciences and Engineering, University of Michigan, Ann

10 Arbor, MI, 48109, USA

11

12 *Corresponding author: William Wieder (wwieder@ucar.edu)

13

14 **Key Points**

15 ● The model simulates low interannual variability of net carbon fluxes due to high
16 covariance of plant productivity and ecosystem respiration
17 ● Dominant modes of variability are characterized by a seasonal amplification and seasonal
18 redistribution of gross primary productivity
19 ● The seasonal redistribution component of carbon cycle variability is a notable feature that
20 appears widespread in the model and observations

21

22 **Abstract**

23 Earth system models are intended to make long-term projections of carbon pools fluxes in
24 response to climate trends, but they can be evaluated on their ability to realistically simulate
25 appropriate carbon cycle sensitivities to climate variability at interannual and seasonal time
26 scales. The Community Earth System Model (CESM2) showed improvements to the
27 representation of the cumulative land carbon sink over the historical period, relative to its
28 predecessor. Our analysis suggests that the interannual variability (IAV) in net terrestrial carbon
29 fluxes simulated by the model did not show similar improvements. The model simulated low
30 IAV of net ecosystem productivity, that also has a weaker than observed climate sensitivity
31 compared to observations. Low IAV likely resulted from a high covariation in gross primary
32 productivity (GPP) and ecosystem respiration. The IAV of GPP had strong climate sensitivities,

33   with positive GPP anomalies associated with warmer and drier conditions in high latitudes, and

34   with wetter and cooler conditions in mid and low latitudes. We identified two dominant modes of

35   variability in GPP anomalies that are characterized by seasonal amplification and redistribution.

36   Climate sensitivities associated with the seasonal amplification of GPP were similar to annual

37   climate anomalies. Seasonal redistribution of GPP fluxes is initiated by springtime temperature

38   anomalies, but subsequently negative feedbacks in soil moisture anomalies during the summer

39   and fall result in negligible changes in the annual GPP flux. These two modes of variability are

40   also seen in remote sensing products, suggesting that CESM2 appropriately represents regional-

41   to-global sensitivities of terrestrial carbon fluxes to climate variability.

42

43   **Plain Language Summary**

44   Earth system models that are intended to make climate change projections also represent the

45   global exchange of carbon dioxide (CO_2) between the atmosphere, ocean and land. As such, the

46   growth rate and variability of CO_2 concentrations in the atmosphere provide a robust

47   measurement to evaluate the representation of the terrestrial carbon cycle in models. We looked

48   at the interannual variability of terrestrial carbon fluxes and their sensitivity to variations in

49   temperature and water that were simulated by the Community Earth System Model (CESM2)

50   and compared them to observations. We found that the model underestimates the interannual

51   variability of net terrestrial carbon fluxes. At the same time, we identified two modes of

52   variability that correspond to an increase in summer productivity (amplification) and a change in

53   the seasonal timing (redistribution) of productivity. Notably, the seasonal redistribution was

54   initialized by warmer springs that increased early-season productivity, but subsequent water

55   limitations in the summer and fall resulted in lower than average productivity and negligible

56   changes in the annual carbon flux. Similar patterns of seasonal amplification and redistribution

57   are seen in satellite observations, suggesting that the model is realistically simulating

58   characteristics of terrestrial ecosystems necessary for capturing carbon-climate feedbacks.

59

1. Introduction

Terrestrial ecosystems continue to provide a sink for about a quarter of anthropogenic carbon dioxide (CO_2) emissions (Ballantyne et al., 2012; Friedlingstein et al., 2019), but the long-term strength and locations of this sink remain uncertain (Gaubert et al., 2019; Tagesson et al., 2020). The net terrestrial flux of CO_2 to or from the atmosphere depends on the balance between much larger carbon fluxes that are driven by plant productivity, ecosystem respiration, and disturbances like fire (Keppel-Aleks et al., 2014). Observational constraints on these gross fluxes are difficult to make globally, which results in persistently high uncertainty in terrestrial carbon cycle projections (Anav et al., 2013; Arora et al., 2020; Friedlingstein et al., 2014). Thus, capturing the appropriate sensitivities to climate driven carbon cycle variability at interannual and seasonal time scales over the observational record may be important to improving longer-term projections of terrestrial carbon balance.

At decadal- to century-time scales, the net exchange of CO_2 between the land and atmosphere remains one of the more robust benchmarks by which to evaluate the representation of terrestrial biogeochemistry in land models (Collier et al., 2018; Hoffman et al., 2014; Keppel-Aleks et al., 2013). Indeed, successive generations of the Community Earth System Model (CESM) and its terrestrial component, the Community Land Model (CLM) show improvements in the globally integrated net terrestrial carbon flux over the historical period (1850-2014; Bonan et al., 2019; Danabasoglu et al., 2020; Lawrence et al., 2019). This suggests that on longer timescales the model adequately represents dominant features influencing in the terrestrial carbon cycle dynamics, namely land-use and land cover change as well as potential CO_2 fertilization effects (Wieder et al., 2019). These longer-term benchmarks, however, offer little insight into the environmental sensitivities of terrestrial CO_2 fluxes, which are important for understanding carbon cycle responses to future climate change.

Measurements of the atmospheric CO_2 growth rate provide an integrated estimate of the interannual variability (IAV) in global carbon cycle (Keeling et al., 1995; Zeng et al., 2005). Since much of the observed IAV is driven by terrestrial processes, variability in the atmospheric CO_2 record provides a top-town constraint on the climate sensitivity of land-atmospheric CO_2 exchange (reviewed by Piao et al., 2020). Specifically, natural climate variability in temperature and precipitation over land are the primary drivers of terrestrial carbon cycle variability that can be inferred from IAV in the atmospheric CO_2 growth rate. This includes the temperature

91   sensitivity of gross primary productivity (GPP) and ecosystem respiration (R_{eco}) on net

92   ecosystem exchange (NEE, calculated as GPP - R_{eco}), especially in the tropics (Anderegg et al.,

93   2015; Ballantyne et al., 2017; Cox et al., 2013; Rödenbeck et al., 2018b; Wang et al., 2013).

94   Meanwhile, other studies emphasize the importance of soil moisture variability on GPP and

95   NEE, especially in arid and semi-arid ecosystems (Anderegg et al., 2015; Humphrey et al., 2018;

96   Poulter et al., 2014). Jung et al. (2017) suggest that compensating moisture driven variation in

97   local-scale gross fluxes (GPP and R_{eco}) as well as spatial compensation in moisture anomalies

98   among regions leaves a dominant temperature-driven signal in the IAV of land-atmosphere CO_2

99   exchange. Regardless of the mechanism, these findings emphasize the need to understand the

100   local and regional drivers of carbon cycle variability at finer temporal resolution.

101   Disentangling the contributions of gross carbon fluxes and their impact on the IAV of

102   NEE remains a challenge. While GPP and R_{eco} anomalies are strongly auto-correlated, mounting

103   evidence suggests that variance in NEE is more strongly correlated with variance in GPP than

104   R_{eco} (Baldocchi et al., 2018; Schwalm et al., 2010). Globally gridded estimates of net and gross

105   carbon fluxes are derived from upscaled flux tower measurements (Beer et al., 2010; Jung et al.,

106   2011; Jung et al., 2017) or remote sensing (Alemohammad et al., 2017; Köhler et al., 2018;

107   Running et al., 2004) either have low, or questionable representation of IAV that may limit their

108   utility in evaluating simulated carbon cycle variability in models (Jung et al., 2020; Piao et al.,

109   2020; Y. Zhang et al., 2018). These remote sensing products, however, do offer promise for

110   diagnosing seasonal carbon cycle responses to climate variability, especially in the extra-tropics

111   (Buermann et al., 2018). Notably, Butterfield et al. (2020) found that while local to regional-

112   scale IAV was poorly correlated among observational data products, they could identify seasonal

113   modes of variability that shared common features and environmental sensitivities. These

114   included the: 1) Amplification of the seasonal cycle of GPP, which was associated with increases

115   in summertime soil moisture availability, and 2) Seasonal redistribution of GPP that was initially

116   driven by warmer springtime temperatures but followed by higher than average soil moisture

117   stress in the summer and fall.

118   Given improvements to the representation of the cumulative land carbon sink over the

119   historical period in CESM2, relative to CESM1 (Danabasoglu et al., 2020), we wanted to

120   investigate the representation of carbon cycle variability at interannual and seasonal timescales in

121   the model. Specifically, our aims were to: 1) Quantify both the IAV of land carbon fluxes

122   simulated by CESM2-esm-hist and their sensitivity to climate variability; 2) Identify modes of

123   seasonal variability in simulated GPP and their likely climate drivers; and 3) Compare the

124   CESM2-esm simulations to results from observational studies, where possible, and identify

125   strengths and weaknesses in the current model implementation.

126

127   **2. Methods**

128   *2.1 Model simulations*

129   We analyzed simulations from the Community Earth System Model, version 2 (CESM2)

130   that couples atmosphere, ocean, land, sea ice, land ice, and river transport components to

131   simulate physical and biogeochemical conditions over historical and future scenarios

132   (Danabasoglu et al., 2020). Of greatest importance for the simulations analyzed here are the

133   atmospheric and land components, which are each briefly described below. The atmosphere

134   model in CESM2 is the Community Atmosphere Model, version 6 (CAM6) which applies the

135   same Finite Volume dynamical core as previous versions of the model, but has numerous

136   changes to the model parameterization (Danabasoglu et al., 2020). Relative to previous versions

137   of the model, CESM2 shows an improvement in its representation of El Niño Southern

138   Oscillation (ENSO) events and their effect on precipitation and temperature anomaly patterns

139   (Meehl et al., 2020). The atmosphere and land models are run at a nominal 1° horizontal

140   resolution (1.25° longitude by 0.9° latitude) and are coupled every 30 minutes.

141   The terrestrial component of CESM2 uses the Community Land Model, version 5

142   (CLM5), which includes a number of updates that are summarized in (Lawrence et al., 2019).

143   Briefly, these developments simulate transient agricultural expansion and land management

144   (Lombardozzi et al., 2020), represent plant hydraulic stress (Kennedy et al., 2019), and improve

145   the representation of plant nitrogen limitation (R. A. Fisher et al., 2019; Wieder et al., 2019). We

146   used the CESM2-esm historical simulations that has active biogeochemical representation of

147   terrestrial carbon and nitrogen cycles and that also simulates the prognostic evolution of

148   atmospheric CO_2 concentrations based on fluxes with oceans and terrestrial ecosystems.

149   As described in Danabasoglu et al. (2020), initial conditions for the land model and ocean

150   model biogeochemical tracers in the non-ESM piControl experiment were generated using spin-

151   up runs of the land and ocean models, respectively. In these spin-up runs, the active atmospheric

152   component was replaced with a data atmosphere that repeatedly cycled through twenty-one years

153   of surface forcing that were extracted from a fully coupled CESM2 experiment. Twenty-one

154   years of forcing were used in order to capture some aspects of interannual variability. The land

155   model spin-up consisted of an accelerated decomposition (AD) mode segment and a subsequent

156   synchronous spin-up segment. These segments were run for 252 and 1701 years respectively.

157   The ocean model spin-up was applied to biogeochemical tracers. The ocean spin-up was run for

158   1029 years and also utilized a Newton-Krylov solver, based on Lindsay (2017) to more

159   completely spin up a subset of the biogeochemical tracers, including the carbon pools. The esm-

160   piControl was initialized from the piControl experiment using an incremental coupling approach.

161   In an intermediate experiment, which was initialized from the piControl experiment, the carbon

162   cycle of the surface components was coupled bidirectionally to a CO_2 tracer in the atmospheric

163   model. This intermediate experiment was run for 80 years, during which the surface

164   biogeochemical parameterizations adjusted to the prognostic atmospheric CO_2. The esm-

165   piControl experiment was initialized with the model state from the end of this intermediate

166   experiment, and the prognostic CO_2 was coupled to the radiative computations in the

167   atmospheric model. The esm-hist experiments analyzed here were initialized from the esm-

168   piControl experiment. The CESM2-esm historical simulations used CMIP6 forcings for

169   anthropogenic emissions, biomass burning, and volcanic SO_2 emissions from 1850-2014

170   described in Danabasoglu et al. (2020) as well as land use and land cover change described in

171   Lawrence et al. (2019) following CMIP6 protocols outlined by Eyring et al. (2016).

172   Using a single ensemble member of CESM2-esm, we focused our analysis on global,

173   regional, and local carbon fluxes that are simulated during the end of the historical period (1960-

174   2014), which overlaps with atmospheric CO_2 measurements. We quantified variability in carbon

175   fluxes at interannual and seasonal time scales and correlated these fluxes with anomalies in

176   climate drivers (temperature and moisture). The model simulates gross fluxes of GPP and R_{eco},

177   with the difference between them representing net ecosystem production (NEP). Positive values

178   for NEP represent net terrestrial ecosystem uptake of carbon. We focused on NEP instead of net

179   ecosystem exchange or net biome production (NEE and NBP, respectively), which include fluxes

180   from fire, land use, and land management, because the CESM2-esm-hist simulations have

181   unrealistically large fire carbon fluxes from land degradation in the tropics at the end of the

182   historical period.

183

184   ***2.2 Statistical Analyses***

185   We summed monthly carbon fluxes (NEP, GPP, and R_{eco}) that were simulated from

186   vegetated terrestrial grid cells to calculate accumulated annual fluxes and weighted them by grid

187   cell area and land fraction to calculate global values. We similarly calculated mean annual

188   temperature (TBOT) and terrestrial water storage (TWS) that was simulated by the model. The

189   CESM2-esm results showed strong long-term trends in relevant variables (Fig. S1), so we

190   subtracted linear trends and focused on the detrended anomalies from the climatological mean

191   state for both monthly and annual data. The IAV was calculated as the standard deviation of

192   annual results simulated from 1960-2014. We compared the IAV in global detrended anomalies

193   of simulated CO_2 fluxes, simulated land CO_2 fluxes, and NEP to those observed in the

194   atmospheric CO_2 growth rate reported by the Global Carbon Project (Friedlingstein et al., 2019).

195   As most of the variability in global CO_2 fluxes is driven by IAV in terrestrial fluxes (Fig. S2), we

196   focus on the IAV of NEP and its component fluxes.

197   To characterize relationships in the data we calculated Pearson's correlation coefficients

198   and regression statistics between detrended anomalies in carbon fluxes, moisture, and

199   temperature. We also calculated the grid cell variance and standard deviation of annual,

200   detrended carbon fluxes to look at covariation between simulated fluxes (as in Baldocchi et al.,

201   2018). We found a robust correlation in the IAV of NEP and its component fluxes, and a strong

202   covariance between GPP and R_{eco} variability. Thus, we focus the remainder of our analysis and

203   discussion on variability in simulated GPP and its environmental sensitivities.

204   To decompose the annual cycle of GPP simulated in each terrestrial grid cell and identify

205   modes of variability we used a singular value decomposition (SVD; Golub & Reinsch, 1971 as in

206   Butterfield et al., 2020). The SVD decomposed the time series of detrended GPP anomalies into

207   singular vectors (SV_i), the elements of which reflect the month (m) of the year (y; Fig. S3).

208   Vectors are ranked by the fraction of variance they explain in the GPP time series. Each singular

209   vector also receives a weight w_i, one per year per singular vector, that quantifies the contribution

210   from an individual singular vector to the observed IAV in any given year. Thus, the simulated

211   IAV time series for a grid cell can be fully reconstructed as the weighted sum of singular vectors:

212

213        $\mathbf{IAV}(y,m) = \Sigma_i\, w_i(y) \times \mathbf{SV}_i(m)$ (1)

214

215   Our SVD had 55 singular vectors (i, corresponding to the number of years in our analysis). We

216   focused on the first two of these to characterize the dominant modes of variability in GPP that

217   are simulated by CESM2-esm. We also calculated a redistribution metric, $\boldsymbol{\theta}$, as the sum of

218   elements from a singular vector divided by the absolute values of the sum of elements from that

219   vector (Butterfield et al. 2020).

220

221        $\boldsymbol{\theta} = \Sigma_m \mathbf{SV}_i(m) / \Sigma_m |\mathbf{SV}_i(m)|$ (2)

222

223   Thus, when $\boldsymbol{\theta} = 0$, GPP was redistributed within the growing season without changing the annual

224   flux. By contrast, values of $\boldsymbol{\theta} = 1$ (or -1) indicate that every month had a positive (or negative)

225   anomaly in GPP relative to the multi-year mean.

226   We identified the mode of variability corresponding to a seasonal amplification of GPP

227   as the vector whose elements most strongly correlated with annual climatology of GPP. The

228   other mode of variability corresponded to a seasonal redistribution of GPP, which typically has

229   both positive and negative phases. The $\boldsymbol{\theta}$ values were used to confirm the appropriate

230   identification of amplification and redistribution modes of variability in each grid cell (e.g.,

231   $|\boldsymbol{\theta}|_{amplification} > |\boldsymbol{\theta}|_{redistribution}$). To facilitate our analysis, we reversed the sign of singular vector

232   elements, weights and $\boldsymbol{\theta}$ values so that amplification vectors were positively correlated with the

233   annual climatology of GPP and the redistribution vector started with a positive phase (Fig. S4).

234   For visualization we calculated regional means for elements in the seasonal amplification and

235   redistribution vectors across high, mid, and low latitude bands in both hemispheres (50-80°, 20-

236   50°, and 0-20°, respectively). Finally, to link modes of carbon cycle variability back to climate

237   anomalies we calculated seasonal means for GPP, air temperature, and terrestrial water storage

238   anomalies. We looked at Pearson's correlation coefficients between these seasonal anomalies

239   and the SVD weights generated for amplification and redistribution vectors.

240

241   **3 Results**

242   *3.1 Interannual variability*

243   Detrended anomalies of terrestrial net ecosystem production (NEP) that are simulated by

244   CESM2-esm have low variability, compared to the atmospheric growth rate of CO_2 measured

245   since 1959 and reported by the Global Carbon Project (Friedlingstein et al., 2019; Figs. 1a, S2).

246   The standard deviation of modeled NEP fluxes (0.47 Pg C y^{-1}) is roughly half of the standard

247   deviation in the observed atmospheric CO_2 growth rate (0.95 Pg C y^{-1}). Note, for convenience we

248   inverted the sign of the atmospheric growth rate so that positive anomalies in Fig. 1a show net

249   land C uptake for both the model and observations. We also note that any temporal correlations

250   between C flux anomalies in CESM2-esm simulations and atmospheric observations here are

251   unintended, because CESM2-esm is experiencing a modeled atmosphere that does not

252   necessarily match local, regional, or global conditions experienced during the historical record of

253   atmospheric CO_2 observations. Figure 1b shows detrended annual anomalies of NEP (as in Fig.

254   1a using a different scale) along with annual anomalies in terrestrial water storage (over

255   vegetated grid cells) and tropical air temperatures over land (23°S - 23°N). The magnitude of

256   terrestrial water storage and tropical air temperature variability simulated in CESM2-esm seems

257   reasonable, compared to observations (σ = 0.82 Tt H_2O and 0.10 K, respectively; Fig. 1b) (Cox

258   et al., 2013; Humphrey et al., 2018). These atmospheric signals, however, do not translate into

259   terrestrial carbon cycle variability.

260

261

262
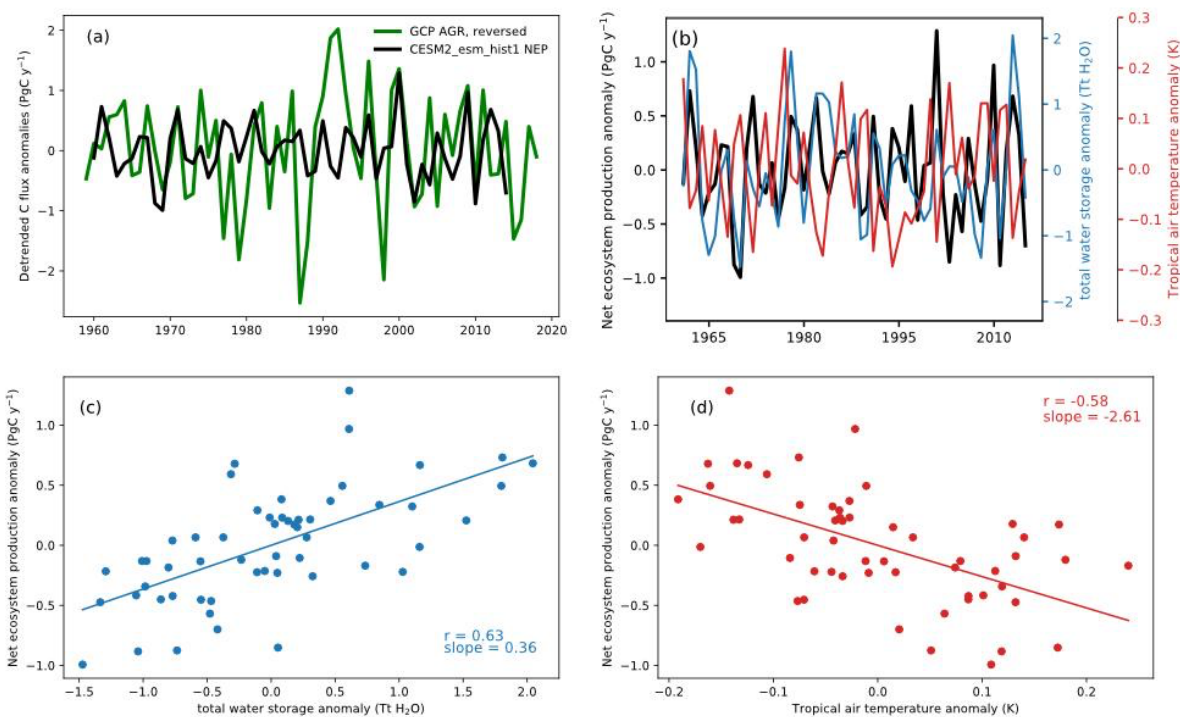
Figure 1. Detrended annual anomalies of global carbon fluxes, climate drivers, and their correlation. Upper panels show: (a) Atmospheric CO_2 growth rate reported by the global carbon project (Friedlingstein et al., 2019) and net ecosystem production (NEP) simulated CESM2-esm (green and black lines, respectively); and (b) NEP, terrestrial water storage (TWS), and tropical air temperature anomalies simulated by CESM2-esm (black, blue, and red lines respectively. Lower panels show correlations between simulated: (c) TWS, which is positively correlated to simulated NEP anomalies; and (d) Tropical air temperature, which is negatively correlated to simulated NEP anomalies. Note, for convenience we inverted the sign of the atmospheric growth rate so that positive anomalies in Fig. 1a show net land C uptake for both the model and observations.

Given the low carbon cycle variability simulated by CESM2-esm (Fig. 1a-b), the model also shows weaker than observed climate sensitivity to global and regional climate anomalies (Fig. 1c-d). The anomalies between NEP and terrestrial water storage are statistically significant (r = 0.63, p<0.001), but with relatively modest effect on carbon cycle variability (slope = 0.36 Pg C y^{-1} Tt H_2O^{-1}), which is weaker than observational estimates from Humphrey et al. (2018; r = 0.85, slope = 1.3 Pg C y^{-1} Tt H_2O^{-1}). We similarly find significant correlations between simulated

281   anomalies of NEP and tropical temperature (r = -0.58, p<0.001, slope = -2.6 Pg C y^{-1} K^{-1}), which

282   is also weaker than observed estimates [Cox et al. (2013), r = -0.65, slope = -5.1 Pg C y^{-1} K^{-1};

283   Wang et al. (2013), r = -0.7, slope = -3.5 Pg C y^{-1} K^{-1}] (see also, Ballantyne et al., 2017;

284   Rödenbeck et al., 2018a).

285   The aggregated use of globally integrated carbon cycle and climate metrics are

286   convenient for comparing atmospheric CO_2 observations, but they do not provide much insight

287   into the mechanism responsible for carbon cycle variability or its spatial structure. The mean of

288   grid cell standard deviations in detrended NEP anomalies simulated from 1960-2015 in CESM2-

289   esm (40.5 g C m^{-2} y^{-1}) was large, relative to the mean of grid cell NEP simulated over this time

290   (39.5 g C m^{-2} y^{-1}). Observed mean and standard deviation of net carbon fluxes from a synthesis

291   of FLUXNET observations by Baldocchi et al. (2018) are much larger than those that are

292   estimated by CESM2-esm (observed net ecosystem exchange = 153 +/- 230 g C m^{-2} y^{-1}; mean ±

293   σ of annual anomalies). Although the network's data coverage is improving, the mismatch in

294   aggregated statistics for the CESM2 and FLUXNET data potentially highlight biases in the

295   spatial distribution of FLUXNET observations to relatively mesic temperate environments

296   (Pastorello et al., 2017).

297   Observed and simulated variability in NEP is driven by variability in component fluxes

298   gross primary productivity (GPP) and ecosystem respiration (R_{eco}). The mean standard deviation

299   of detrended GPP and R_{eco} anomalies (102 and 83.8 g C m^{-2} y^{-1}, respectively) in CESM2 were

300   about 10% of the mean fluxes (950 and 910 g C m^{-2} y^{-1}, respectively). The grid cell variance of

301   NEP was strongly and positively correlated with the variance of component fluxes (Fig. 2a).

302   Although variance in NEP is slightly better explained by GPP variance (r = 0.79, slope = 0.77)

303   than R_{eco} variance (r = 0.74, slope = 0.72; Fig. 2a), the anomalies of the component fluxes are

304   highly correlated with each other (r = 0.94, slope = 0.80; Fig. 2b). By contrast, observations from

305   FLUXNET show lower correlations between GPP and R_{eco} anomalies (r = 0.70, slope = 0.42;

306   Baldocchi et al. 2018). The strong simulated correlation between simulated GPP and R_{eco} likely

307   accounts for some of the low interannual variability in land carbon uptake in CESM2, since years

308   with large GPP fluxes are necessarily compensated by R_{eco} fluxes that are of nearly the same

309   magnitude. Given strong correlations between GPP and R_{eco} fluxes, we focus the remainder of

310   our analysis on patterns in GPP variability and its response to moisture and temperature
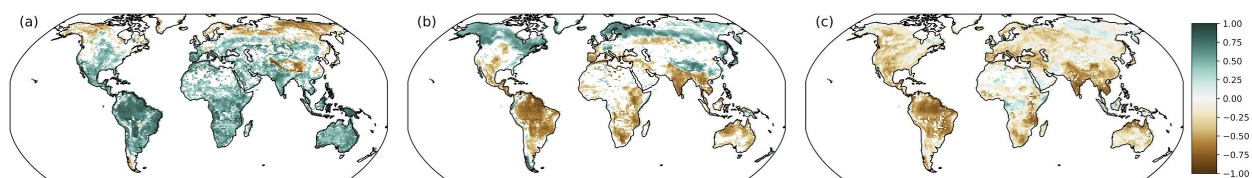
311   anomalies.
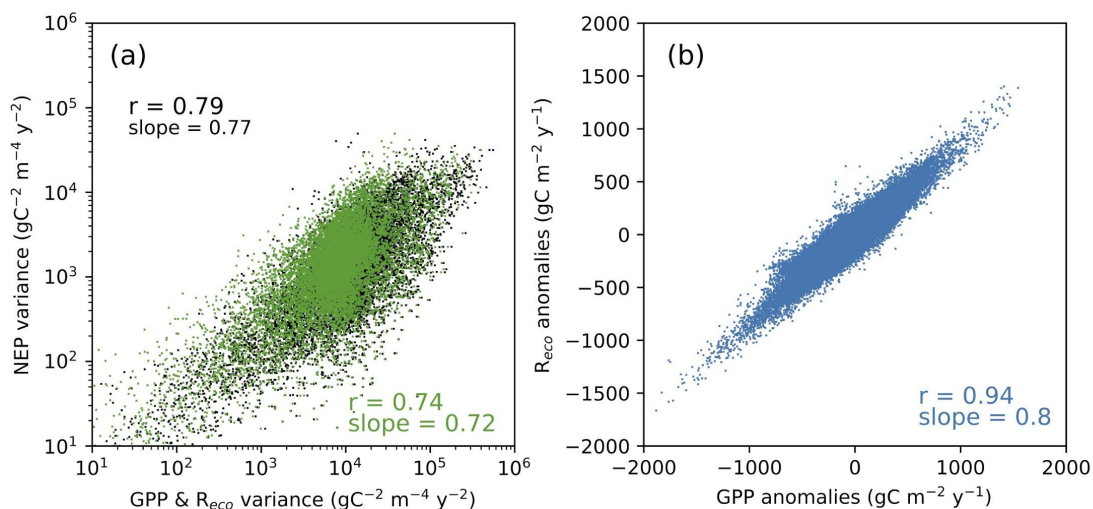
Figure 2. Correlations of grid cell carbon fluxes simulated by CESM2-esm from 1960-2015: (a) Variance in NEP versus GPP and R_{eco} (shown in black and green, respectively); and (b) Autocorrelation of anomalies in R_{eco} and GPP. Pearson correlation coefficients and regression slopes from each relationship are provided in each panel, all correlations are significant ($p < 0.001$).

The standard deviation of detrended annual GPP anomalies shows high variability in tropical savannah regions, but relatively low variance in highly productive tropical forests (Fig. S5a). When normalized for mean annual GPP, the low productivity regions show higher coefficient of variation (CV), while higher productivity forests show relatively low CV in plant productivity (Fig. S5b-c). In Table S1 we compared the coefficients of variability (defined as the ratio of the interannual standard deviations to the seasonal amplitude of the multi-year mean) in four ecoregions of North America as defined in Butterfield et al. (2020) from CESM2 and several remote sensing products. The various remote sensing products show a factor of two difference in the range of variability in regional GPP estimates, and the magnitude of GPP variability simulated by CESM2 is comparable to these observationally derived estimates. This finding contradicts results reported by Wozniak et al. (2020), who found lower than observed variability in land-only simulations conducted with CLM5 at flux tower sites.

The IAV of detrended GPP anomalies simulated in CESM2 is positively correlated with terrestrial water storage anomalies in low and mid latitude regions (50°S - 50°N), whereas high latitude systems show a negative correlation between GPP and water storage anomalies (Fig. 3a).

334   In general, arid and savannah regions on nearly every continent show strong positive correlations

335   in the IAV of GPP with terrestrial water storage, except for parts of the Western United States.

336   These patterns are reversed for correlations between GPP and air temperature anomalies (Fig.

337   3b). Over cold regions, and especially in boreal forests, the IAV of detrended GPP anomalies are

338   positively correlated with air temperature anomalies. By contrast, over mid and low latitudes,

339   especially in the Amazon, SE Asia, and N Australia, the IAV of detrended GPP anomalies are

340   negatively correlated with air temperature anomalies. Finally, although many regions show

341   strong, negative correlations between terrestrial water storage and temperature anomalies (e.g.,

342   the Americas, SE Asia, and Australia), other regions show positive correlations between these

343   simulated climate anomalies (e.g., parts of tropical Africa, tropical Asia, and the high Arctic; Fig

344   3c).

345

346

347   **Figure 3.** Correlations coefficients between detrended annual anomalies that are simulated by

348   CESM2-esm from 1960-2014. Panels show the correlation between (a) GPP and terrestrial water

349   storage; (b) GPP and air temperature; and (c) terrestrial water storage and air temperature. Only

350   statistically significant correlations ($p < 0.05$, when $|r| > 0.226$ for 55 years of data) are shown.

351

352   ***3.2 Seasonal variability***

353   The first two vectors in the singular value decomposition explained 75% (area weighted

354   mean) of the variance in GPP over the vegetated land surface. In general, the amplification

355   vector explained the greatest fraction of variance in GPP, especially in arctic and arid regions

356   (global area weighted mean = 45%; Fig. 4a). The redistribution vector explained the largest

357   fraction of variation over more mesic regions in the mid latitudes (global weighted mean = 29%;

358   Fig. 4b). Neither vector explained a large fraction of GPP variance over tropical forests, which

359   generally showed low variability in detrended GPP anomalies (Fig. S5).

360
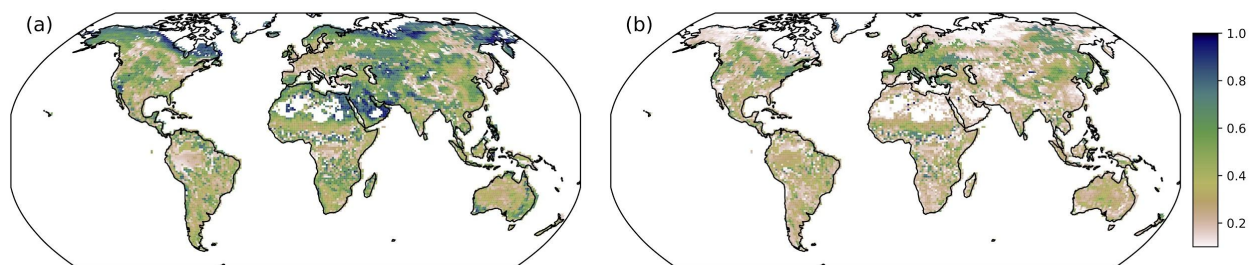
Figure 4. Fraction of variance in detrended GPP anomalies that was explained by (a) seasonal amplification or (b) seasonal redistribution vectors.

Figure 5 shows the mean annual climatology of the GPP, as well as the monthly values for amplification and redistribution vectors (grey, blue, and red lines respectively) for latitudinal bins. High and mid latitudes are characterized by a strong annual cycle of GPP that is strongly correlated with the amplification vectors describing GPP variability (Fig. 5a, b, e). The amplification vector describes 56%, 45%, and 38% of the GPP variability in arctic, northern hemisphere temperate, and southern hemisphere temperate latitudinal zones, respectively. By contrast, the redistribution vectors in these regions explain 26-31% of the GPP variability and are characterized by positive spring-time anomalies that are followed by negative summer and fall anomalies. In the tropics, the seasonal cycle is more muted, but seasonal amplification and redistribution vectors describe roughly 40% and 30% of the variability in GPP, respectively (Fig. 5 c, d). The θ values calculated in the SVD show the net impact on the integrated seasonal signal of GPP. The mean θ values associated with the amplification vector are globally positive (Fig. 5). By contrast, the θ values associated with a seasonal redistribution of GPP are close to zero, indicating little to no change in integrated seasonal signal of GPP from seasonal redistribution of GPP. Thus, although the seasonal redistribution of carbon variability is a major source of global carbon cycle variability in the model, it would not be evident in more aggregated metrics of variability that only look at annual times-scales (e.g., Fig. 1).
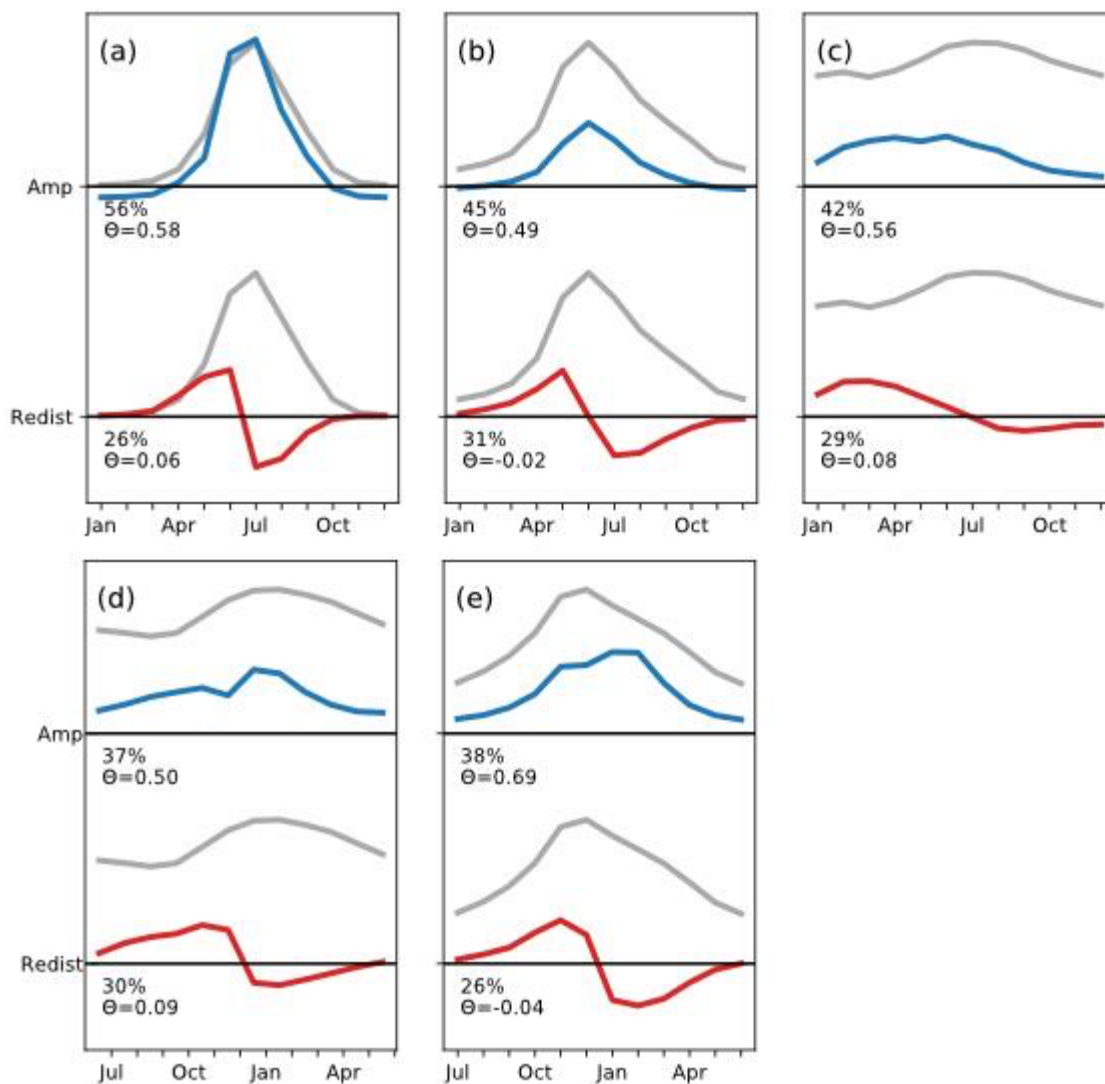
Figure 5. Zonal mean climatology of monthly GPP and singular vectors associated with seasonal amplification and redistribution of GPP (grey, blue, and red lines respectively) for the northern hemisphere and southern hemisphere (top and bottom rows, respectively). Panels show: (a) high latitude ecosystems, 50-80°N; (b) northern temperate mid latitudes, 20-50°N; (c-d) tropics, 0-20°N and 0-20°S, respectively; and (e) southern temperate mid latitudes, 20-50°S. The magnitude of the singular vectors is arbitrary (y-axis). Mean fraction of variance explained and θ values, which indicate the net impact on the integrated seasonal signal of GPP for each singular vector, are also provided. Note x-axis was shifted for southern hemisphere plots to show the climatology for austral summer.

394   To evaluate the environmental drivers of GPP variability we conducted linear regressions

395   on the weights from the amplification (Fig. 6) and redistribution (Fig. 7) vectors from SVD

396   analysis (n = 55, for each year of the simulation) with seasonal anomalies of GPP, terrestrial

397   water storage, and air temperature. The SVD weights for the amplification vector were strongly

398   and positively correlated with the GPP anomalies during the peak of the growing season (Fig. 6,

399   left column). This is expected, since the amplification vector was identified by its correlations

400   with the climatology of GPP, so correlation coefficients are highest in the summer months (JJA

401   and DJF for northern and southern hemispheres, respectively). Strong correlations are evident at

402   other times (e.g., negative correlations between weights and GPP anomalies across high latitudes

403   in DJF), but the magnitude of these anomalies is small relative to the annual cycle (see also Fig.

404   5a). Although terrestrial water storage and air temperature are auto-correlated (Fig. 3), high-

405   latitude ecosystems generally show SVD amplification weights that are more positively

406   correlated with air temperature anomalies and negatively correlated with water storage anomalies

407   in JJA (Fig. 6, right and middle columns, Table S2). By contrast, SVD amplification weights are

408   more strongly and positively correlated with wetter-than-average conditions across mid and low

409   latitudes, and negatively correlated with air temperature anomalies.

410
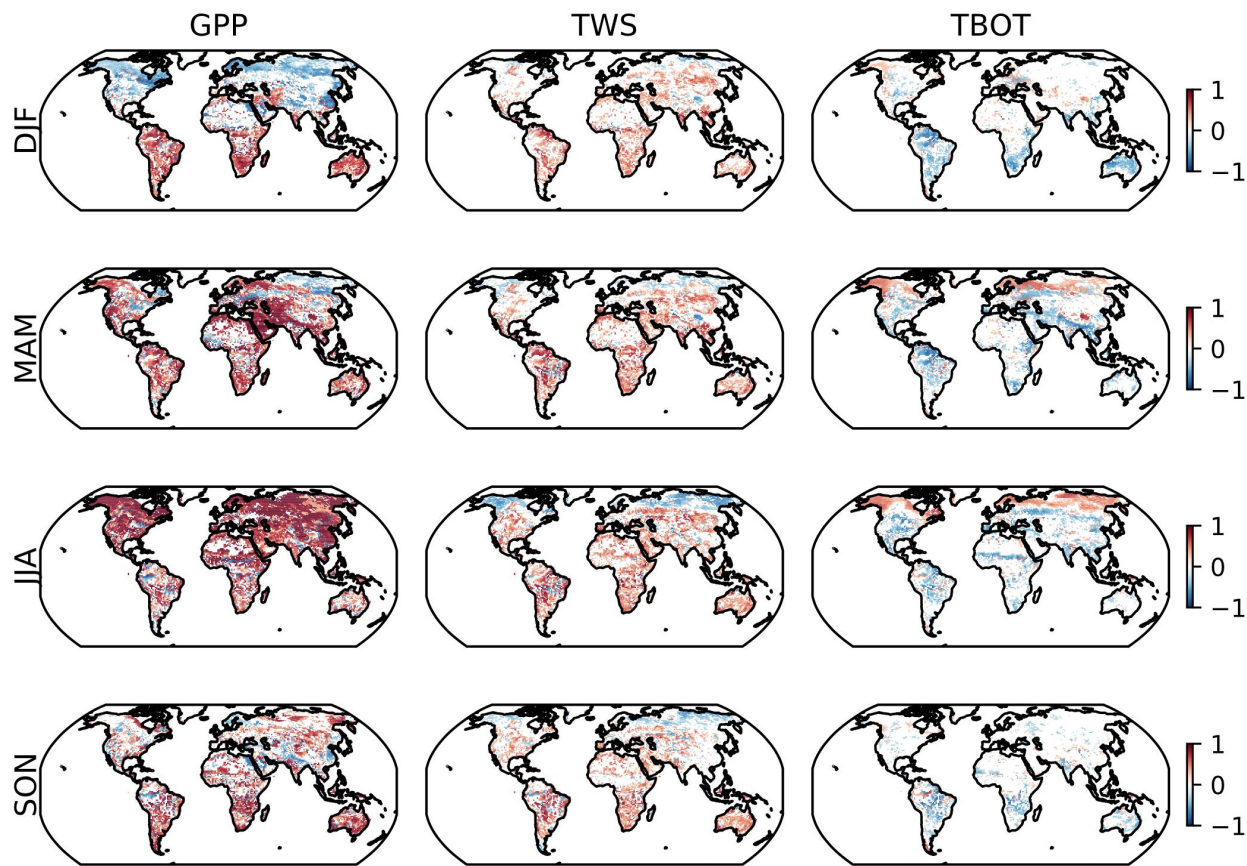
Figure 6. Pearson correlation coefficients between SVD weights from the amplification vector with seasonal anomalies of GPP, terrestrial water storage (TWS), and air temperature (TBOT) simulated by CESM2-esm from 1960-2014. Only statistically significant ($p < 0.05$) correlations are shown ($|r| > 0.26$, two-tailed test, $n = 55$).

The SVD weights for the redistribution vector were strongly and positively correlated with the GPP anomalies during the spring, with correlation coefficients that are highest in the MAM and SON (for northern and southern hemispheres, respectively; Fig. 7, left column). In the northern hemisphere, the positive phase of the redistribution vector is also more strongly correlated with warmer spring-time air temperatures (Fig. 7, right column) than terrestrial water storage. Subsequent GPP anomalies in the summer and fall, however, show negative correlations with SVD weights (see also Fig. 5). In the summer (JJA) these periods are still characterized by warmer, but also drier than average conditions (Fig. 7, middle column; Table S3). By fall (SON), negative GPP anomalies are only associated with drier than average conditions.
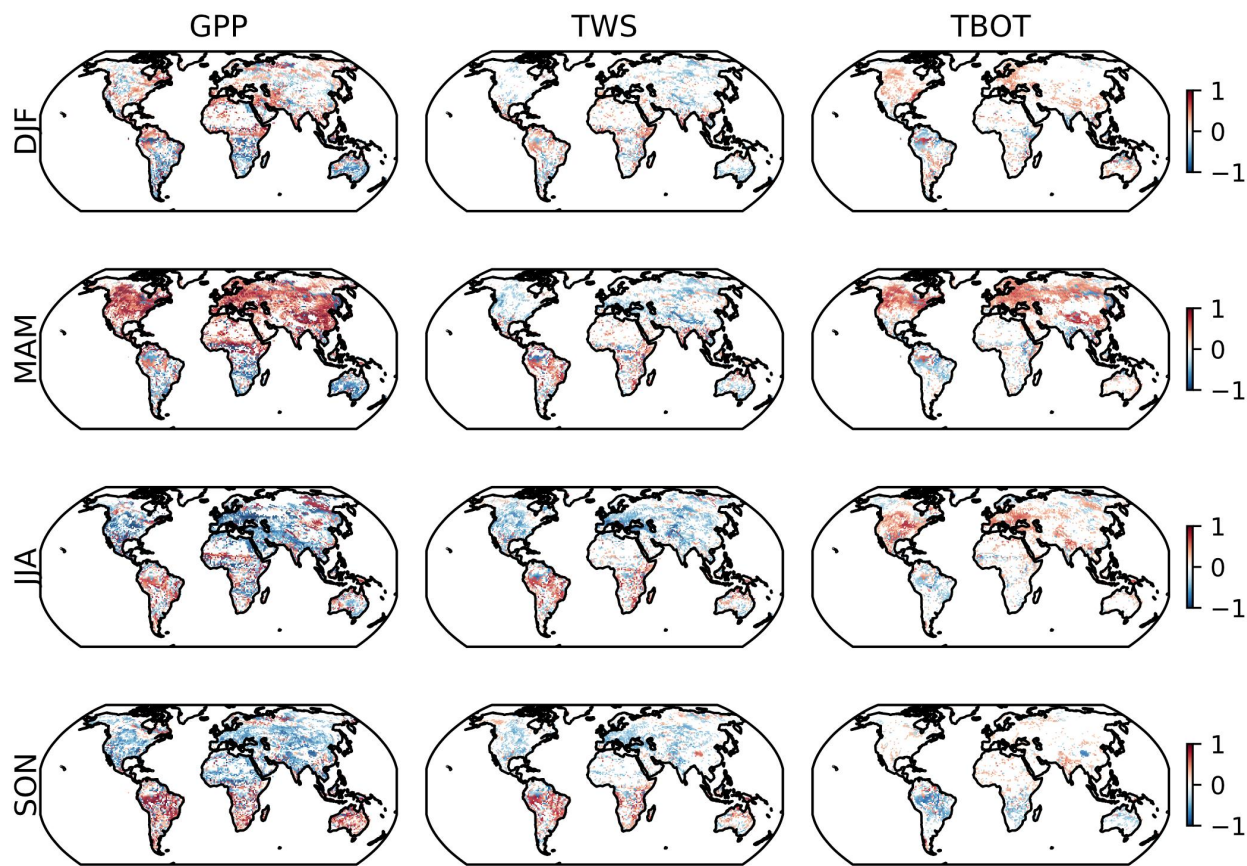
Figure 7. Pearson correlation coefficients between SVD weights from the redistribution vector with seasonal anomalies of GPP, terrestrial water storage (TWS), and air temperature (TBOT) simulated by CESM2-esm from 1960-2014. Only statistically significant ($p < 0.05$) correlations are shown ($|r| > 0.26$, two-tailed test, $n = 55$).

4. Discussion

4.1 Interannual variability

Our results show that the magnitude of global carbon cycle variability simulated by CESM2-esm is low, relative to measurements of IAV in the atmospheric CO_2 growth rate (Fig. 1). Observed variation in the atmospheric CO_2 growth rate shows strong reductions in land carbon uptake during the 1987 and 1998 ENSO events, as well as strong increases in land carbon uptake associated with the 1992 Pinatubo eruption (Fig. 1a). The CESM2 has a good representation of precipitation and temperature anomaly patterns associated with tropical Pacific sea surface temperatures (Danabasoglu et al., 2020; Meehl et al., 2020), and is forced with observed volcanic aerosols during the historical period (Fig. S2). Accordingly, the magnitude of

441   terrestrial water storage and air temperature variability agrees reasonably well with observations

442   (Fig. 1; Cox et al., 2013; Humphrey et al., 2018). This suggests that the model adequately

443   represents global-scale climate variability, but that this climate variability does not generate

444   enough terrestrial carbon cycle variability in the model.

445   Since the atmosphere and land models are coupled in the CESM2-esm simulations, we do

446   not expect the timing of ENSO events to line up with observations. As such, the comparison

447   between NEP and terrestrial water storage and NEP and air temperature anomalies are more

448   illustrative of the relationship between observed atmospheric CO_2 growth rates and climate

449   variability (Fig. 1c, d). Note, the sign of relationships from previously published work was

450   reversed so that positive carbon flux anomalies reflect terrestrial carbon uptake, as in Figure 1.

451   We appreciate that all of these studies use slightly different time periods for their calculations,

452   but we do not expect this to significantly alter the fundamental sensitivities of land carbon fluxes

453   to climate variability. Indeed, these findings are generally consistent with land-only simulations

454   using the Community Land Model (CLM5), which also shows weaker than observed carbon

455   cycle variability when driven by reanalysis climate forcing data that reflects the historical drivers

456   of the observed carbon cycle variations (Lawrence et al., 2019).

457   Coupled Earth system models would ideally simulate relationships between the carbon

458   cycle and climate variations over a range of spatial scales. Ultimately, the long-term CO_2

459   forcing reflects the global integral of local to regional carbon-climate feedbacks. To diagnose

460   this global signal, atmospheric CO_2 observation and inversion models provide one approach to

461   evaluating model simulations that can provide insight into regional drivers of CO_2 variability

462   (Keppel-Aleks et al., 2014), but they are characterized by large uncertainties that limit their

463   utility to detect proximal causes of carbon cycle variability. Our work finds that plant

464   productivity simulated by CESM2-esm shows distinct regional signatures in climate sensitivity

465   and variability at annual and seasonal timescales that imprint onto the net land carbon flux.

466   In contrast, local-scale observations provide a bottom-up perspective on sources of

467   carbon cycle IAV. Indeed, observations from eddy-covariance towers have long-been used to

468   evaluate land models (Baldocchi et al., 2001; Bonan et al., 2012; Melaas et al., 2013; Pastorello

469   et al., 2017). Measurements from multiple tower sites, therefore, provide another means to

470   evaluate carbon cycle simulations. Syntheses from FLUXNET observations show larger net

471   carbon fluxes and greater variability than CESM2-esm simulations (Fig. 2a; Baldocchi et al.,

472   2018). A number of factors – including differences in atmospheric conditions, spatial coverage,

473   temporal extent, and potential legacy effects – may lead to mismatches in flux tower

474   observations and coupled Earth system model output (Raczka et al., 2013). Caveats aside, the

475   FLUXNET observations are consistent with atmospheric CO_2 measurements and suggest that

476   CESM2 underestimates the IAV of land carbon uptake (Figs. 1-2), prompting us to look more

477   closely at the components of terrestrial carbon fluxes that may be responsible for this feature in

478   the model.

479   The IAV in net carbon fluxes results from variability in component fluxes (GPP and R_{eco})

480   and their interaction (Baldocchi et al., 2018; Lasslop et al., 2010). Our results suggest that

481   CESM2-esm shows notably low IAV of GPP fluxes in tropical forests (Fig. S5). Similarly, in

482   temperate deciduous forests, Wozniak et al. (2020) found that maximum rates of GPP simulated

483   by CLM were much lower than observations at a number of AmeriFlux sites. Indeed,

484   measurements from flux towers suggest that brief periods of large photosynthetic uptake appear

485   to be an important component of the IAV in net carbon exchange, especially in arid ecosystems

486   (Fu et al., 2019; Kannenberg et al., 2020). The failure of CLM5 to capture this behavior suggests

487   that the model needs parametric or structural changes in its representation of leaf-level

488   photosynthesis, stomatal conductance, or canopy scaling to capture photosynthetic variability.

489   Beyond the site level, however, regional analyses suggest that the variation in GPP fluxes may

490   be appropriate to a suite remote sensing estimates in the northern hemisphere (Table S1;

491   Butterfield et al., 2020). Additional work is needed to evaluate the utility of detecting IAV of

492   carbon cycle metrics in remote sensing products to further evaluate model simulations, especially

493   in the tropics.

494   Observations suggest that site-level variance in net carbon fluxes is more tightly

495   correlated with GPP than R_{eco} (Baldocchi et al., 2018). By contrast, the CESM2-esm results

496   show strong correlations between NEP and both of its component fluxes (Fig. 2a). Moreover, the

497   anomalies of GPP and R_{eco} that are simulated by CESM2 are more strongly correlated than

498   observations suggest (Fig 2b, Baldocchi et al., 2018). This high covariation between GPP and

499   R_{eco} offsets variance in either of the component fluxes and dampens the IAV of NEP in the

500   model. These results also suggest that the current structure and parameterization of CESM2-esm,

501   which dictates the high covariance of simulated GPP and R_{eco} should likely be evaluated and

502   revised. We suspect that several changes made to the land model for CESM2 are likely

503   responsible for the high covariation of GPP and R_{eco}. First, CLM5 reduced the magnitude of

504   growth respiration fluxes (Atkin et al., 2017) and reduced the total magnitude of growth and

505   maintenance respiration fluxes, relative to previous versions of the model (Lawrence et al.,

506   2019). Second, the incorporation of the Fixation and Uptake of Nitrogen model (FUN) into

507   CLM5 makes plants pay the carbon costs of nitrogen uptake (FUN; J. B. Fisher et al., 2010; R.

508   A. Fisher et al., 2019; Shi et al., 2016). As currently applied in CLM5, the FUN carbon costs

509   make up a large fraction of autotrophic respiration fluxes and are highly correlated with the

510   timing of GPP. Finally, the parameterization for soil organic matter turnover uses a higher

511   minimum water potential, which increases the sensitivity of heterotrophic respiration fluxes to

512   liquid soil water availability (Carvalhais et al., 2014; Koven et al., 2017; Lawrence et al., 2019).

513   Independently, these changes seem justified in their aim to more realistically represent terrestrial

514   ecosystems, but together they likely served to reduce the IAV of net carbon fluxes that are

515   simulated by CESM2.

516   The IAV of detrended GPP anomalies in CESM2-esm shows strong latitudinal patterns

517   (Fig. 3). Notably, correlations between the IAV of GPP and terrestrial water storage anomalies

518   are particularly strong in many arid, semi-arid and savannah regions (Fig. 3a), a finding that is

519   consistent with work emphasizing moisture and precipitation controls over carbon cycle

520   variability in arid regions (Ahlström et al., 2015; Humphrey et al., 2018; Poulter et al., 2014).

521   Concurrently, correlations between the IAV of GPP and air temperature anomalies are stronger

522   in arctic, boreal and temperate deciduous forests (Fig. 3b), which again is consistent with

523   observations (discussed in section 4.2; Hu et al., 2019; Rödenbeck et al., 2018b). We recognize

524   that inferring the relative importance of climate controls over land-atmosphere carbon exchange

525   remain actively discussed in the literature (Cox et al., 2013; Humphrey et al., 2018; Jung et al.,

526   2017; Piao et al., 2020; Poulter et al., 2014), but given the spatial and temporal heterogeneity of

527   climate anomalies and timescales of ecosystem responses (Rödenbeck et al., 2018b; X. Zhang et

528   al., 2013) we further investigate the seasonal modes of GPP variability that are simulated by

529   CESM2 and their environmental covariates.

530

4.2 Seasonal variability

532   The timing of climate variations with respect to the climatological annual cycle plays an

533   important role in the resulting interannual variability of terrestrial carbons fluxes (Buermann et

534   al., 2018). Satellite and flux tower observations in North America suggest that carbon cycle

535   variability can be decomposed into modes of variability that are characterized by the

536   amplification and redistribution of seasonal fluxes (Butterfield et al., 2020; Byrne et al., 2020).

537   Results from our SVD analysis identified similar modes of variability in GPP that are simulated

538   in CESM2; with amplification vectors dominant in high latitude and arid ecosystems (Fig. 4a)

539   and redistribution vectors that are dominant in temperate forests, boreal forests, and agricultural

540   regions (Fig. 4b). Qualitatively, these patterns align with findings from (Butterfield et al., 2020)

541   who found robust patterns in seasonal variability from several satellite datasets that are

542   correlated with regional anomalies of temperature and soil moisture availability. The seasonal

543   redistribution vector explains a significant amount of carbon cycle variability in CESM2-esm

544   (Figs. 4-5) but would not lead to changes in annual C fluxes ($\boldsymbol{\theta} \sim 0$). Thus, climate effects on this

545   mode of variability would be obscured in quantification of variability on annual time scales. This

546   also suggests that the representation of plant phenology and water stress in CESM2 are likely

547   responding in physically and ecologically realistic ways to simulated climate variability.

548   The nature of carbon cycle variability changes as a function of mean climate, ecosystem

549   type, and the phase of the annual cycle of GPP. In grid cells where the seasonal amplification of

550   GPP characterizes most of the flux variability the second vector from the SVD corresponds to a

551   seasonal redistribution of the fluxes (Figs. 4-5). For example, in high latitude ecosystems the

552   amplification vector describes more than half of the variability in simulated GPP and is

553   associated with a net increase (or decrease) in annual carbon fluxes (Fig. 5a). The weights

554   associated with the amplification vectors are most strongly correlated with summertime GPP

555   anomalies (Fig. 6, top row; Table S2), which is not surprising since we identified the

556   amplification vector from the SVD by its correlation with the mean climatology of monthly GPP

557   fluxes simulated in each grid cell (section 2.2; Fig. S4). The weights from the amplification

558   vectors in high latitude ecosystems show a strong, positive correlation with summertime air

559   temperature anomalies and a weaker, but still significant, negative correlation with terrestrial

560   water storage anomalies. Thus, with warmer (and drier) summertime conditions, CESM2

561   simulated positive GPP anomalies in Arctic and Boreal ecosystems. Conversely, with cooler (and

562   wetter) summertime conditions CESM2 simulated negative GPP anomalies in these regions. Our

563   analysis cannot diagnose the proximal driver of the GPP anomalies, but given their higher

564   correlation coefficient we assume that summertime temperature anomalies are driving the carbon

565 cycle response, with declines in soil moisture subsequently resulting from higher

566 evapotranspiration fluxes in warmer, more productive years.

567   The amplification vector also describes a high fraction of the GPP variability in lower

568 latitudes (Fig. 5b-e). The weights from the amplification vectors in mid and low latitudes shows

569 a strong positive correlation with regional peak growing season GPP anomalies in their

570 respective hemispheres (Fig. 6). In contrast to northern high latitudes, weights from

571 amplification vectors in these regions generally show stronger correlations with terrestrial water

572 storage anomalies than they do for air temperature (Fig. 6, Table S2). Thus, in mid and lower

573 latitudes wetter (and cooler) anomalies during the growing season maxima are associated with

574 positive GPP anomalies, whereas drier (and warmer) anomalies are associated with negative

575 GPP anomalies. While seasonal amplification vectors do explain a majority of the global

576 variability in simulated GPP fluxes, some regions are better characterized by a seasonal

577 redistribution of carbon fluxes that do not necessarily change the annual flux of GPP from the

578 atmosphere onto land, just its timing.

579   The seasonal redistribution of plant productivity explains roughly a quarter of global GPP

580 variability, but this is the dominant form of variability simulated by CESM2-esm in several

581 regions, including the Canadian Great Plains, temperate forests, and agricultural regions (Fig.

582 4b). The seasonal redistribution vector is characterized by positive (or negative) GPP anomalies

583 early in the growing season, followed by GPP anomalies of the opposite sign later in the growing

584 season (Fig. 5). The spatial cohesiveness of this pattern is most notable in the northern

585 hemisphere, where SVD weights associated with the redistribution vector are positively

586 correlated with GPP anomalies and air temperature anomalies in the spring (MAM; Fig. 7). The

587 SVD weights are negatively correlated with GPP and terrestrial water storage anomalies by

588 summer and fall (JJA and SON; Fig 7, Table S3). Drier summer and fall conditions could result

589 from higher evapotranspiration in the spring, or also from increased early runoff due to earlier

590 snowmelt during warm springs (Buermann et al., 2013). Thus, the potential increases in plant

591 productivity from an early green-up that were facilitated by warmer spring temperatures are

592 negated by soil moisture stress later in the growing season, leading to negligible net changes in

593 the annual land carbon flux (mean $\boldsymbol{\theta}$ values close to zero for the redistribution vector; Fig. 5).

594   The regions where a seasonal redistribution vector dominates GPP variability in CESM2-

595 esm (Fig. 4) are also regions where native vegetation in the model use a stress deciduous

596   phenology scheme, or they are under agricultural management, which is explicitly represented in

597   CESM2 (Lawrence et al., 2019; Lombardozzi et al., 2020). Both of these phenology modes use a

598   growing degree day approach to simulate leaf emergence (or planting date and leaf emergence

599   for the CLM5 crop model), so the strong correlation between air temperature anomalies and

600   SVD weights are expected (Fig. 7, Table S3). We were more surprised, however, by the negative

601   GPP anomalies that emerge later in the growing season. These seem to be driven by drier and

602   warmer than average conditions that are consistent with satellite observations of vegetation

603   greenness (Buermann et al., 2013; Buermann et al., 2018). Notably, redistribution vectors in SIF

604   derived GPP in North America are tightly linked with spring (and summer) temperature

605   anomalies, and tend to be stronger in temperate forests, the Canadian Prairies, and agricultural

606   regions (Butterfield et al., 2020; Byrne et al., 2020). The larger influence of seasonal

607   redistribution at lower latitudes that is simulated in CESM2-esm is also consistent with

608   observations from forests reported in (Butterfield et al., 2020), but the overall importance of

609   seasonal redistribution vs. amplification on carbon cycle variability remains uncertain. Indeed,

610   considering the relative importance of these modes of variability may be important in trying to

611   infer appropriate sensitivities and interactions between seasonal to interannual variability in

612   climate, phenology, and ecosystem carbon fluxes from both models and observations.

613

614

615   **5. Conclusion**

616   The interannual variability of terrestrial net carbon exchange with the atmosphere in

617   CESM2-esm is low. Accordingly, the model also simulates a weaker than observed sensitivity of

618   net carbon exchange to global climate anomalies. This low variability of net carbon fluxes likely

619   results from a high covariation in component fluxes of NEP, namely gross primary productivity

620   and ecosystem respiration. The model also may simulate low variability in GPP, especially in the

621   tropics, which may be caused by missing the brief periods of high productivity that are evident in

622   flux tower observations and seem to make an important contribution to carbon cycle IAV. The

623   variability in GPP that is simulated by the model generally shows a latitudinal gradient in climate

624   sensitivities whereby positive GPP anomalies are driven by warmer and drier conditions in high-

625   latitude ecosystems but wetter and cooler conditions in mid and low latitudes.

626   Our analysis decomposes IAV in GPP fluxes into modes of variability, characterized by

627   seasonal amplification and redistribution vectors that together explain three quarters of the global

628   variability in GPP. The seasonal redistribution component to carbon cycle variability is notable

629   because although it is not apparent in more aggregated (annual) measurements of IAV, it does

630   seem widespread in both in the model and in observations. Decomposing carbon cycle variability

631   with the SVD allows us to look at regional patterns that may be consistent with observational

632   data. For example, both the model and observations show that wetter and cooler springs and

633   summers lead to an amplification signal in GPP over the western United States, whereas a

634   temporal redistribution of GPP anomalies is more strongly associated with variability in

635   springtime temperatures in the eastern US. Thus, while the total magnitude of net and gross

636   terrestrial carbon flux variability simulated by CESM2 may be too low, the simulated interannual

637   and seasonal variability does qualitatively capture patterns of regional and global sensitivies to

638   climate variability. More broadly, we contend this kind of analysis is useful in diagnosing

639   strengths and weaknesses in biogeochemical models in comparison to observational data.

640

657 Grid Federation (ESGF; at https://esgf-node.llnl.gov/search/cmip6/, search for CESM2.esm-hist)

658 or from the NCAR Digital Asset Services Hub (DASH; at data.ucar.edu) or from the links

659 provided from the CESM website (at www.cesm.ucar.edu); CESM2 (2019). Code for the

660 analyses presented can be found at WRW's GitHub page

661 (https://github.com/wwieder/ctsm_py/blob/master/notebooks/esmIAV.ipynb), which has been

662 archived at https://doi.org/10.5281/zenodo.4009510.

663

Author contribution

665 WRW conducted the analyses with help from ZB and GKA. WRW wrote the manuscript with

666 contributions from all other authors.

667

References

669 Ahlström, A., Raupach, M. R., Schurgers, G., Smith, B., Arneth, A., Jung, M., et al. (2015). The
670   dominant role of semi-arid ecosystems in the trend and variability of the land CO_2
671   sink. *Science, 348*(6237), 895-899. doi: 10.1126/science.aaa1668.
672 Alemohammad, S. H., Fang, B., Konings, A. G., Aires, F., Green, J. K., Kolassa, J., et al. (2017). Water,
673   Energy, and Carbon with Artificial Neural Networks (WECANN): A statistically-based estimate
674   of global surface turbulent fluxes and gross primary productivity using solar-induced
675   fluorescence. *Biogeosciences, 14*(18), 4101-4124. doi: 10.5194/bg-14-4101-2017.
676 Anav, A., Friedlingstein, P., Kidston, M., Bopp, L., Ciais, P., Cox, P., et al. (2013). Evaluating the Land
677   and Ocean Components of the Global Carbon Cycle in the CMIP5 Earth System Models. *Journal
678   of Climate, 26*(18), 6801-6843. doi: 10.1175/jcli-d-12-00417.1.
679 Anderegg, W. R. L., Ballantyne, A. P., Smith, W. K., Majkut, J., Rabin, S., Beaulieu, C., et al. (2015).
680   Tropical nighttime warming as a dominant driver of variability in the terrestrial carbon sink.
681   *Proceedings of the National Academy of Sciences, 112*(51), 15591-15596. doi:
682   10.1073/pnas.1521479112.
683 Arora, V. K., Katavouta, A., Williams, R. G., Jones, C. D., Brovkin, V., Friedlingstein, P., et al. (2020).
684   Carbon–concentration and carbon–climate feedbacks in CMIP6 models and their comparison to
685   CMIP5 models. *Biogeosciences, 17*(16), 4173-4222. doi: 10.5194/bg-17-4173-2020.
686 Atkin, O. K., Bahar, N. H. A., Bloomfield, K. J., Griffin, K. L., Heskel, M. A., Huntingford, C., et al.
687   (2017). Leaf Respiration in Terrestrial Biosphere Models. In G. Tcherkez & J. Ghashghaie (Eds.),
688   *Plant Respiration: Metabolic Fluxes and Carbon Balance* (pp. 107-142). Cham: Springer
689   International Publishing.
690 Baldocchi, D., Chu, H., & Reichstein, M. (2018). Inter-annual variability of net and gross ecosystem
691   carbon fluxes: A review. *Agricultural And Forest Meteorology, 249*, 520-533. doi:
692   10.1016/j.agrformet.2017.05.015.
693 Baldocchi, D., Falge, E., Gu, L., Olson, R., Hollinger, D., Running, S., et al. (2001). FLUXNET: A New
694   Tool to Study the Temporal and Spatial Variability of Ecosystem–Scale Carbon Dioxide, Water
695   Vapor, and Energy Flux Densities. *Bulletin of the American Meteorological Society, 82*(11),
696   2415-2434. doi: 10.1175/1520-0477(2001)082<2415:Fantts>2.3.Co;2.
697 Ballantyne, A. P., Alden, C. B., Miller, J. B., Tans, P. P., & White, J. W. (2012). Increase in observed net
698   carbon dioxide uptake by land and oceans during the past 50 years. *Nature, 488*(7409), 70-72.
699   doi: 10.1038/nature11299.

Ballantyne, A. P., Smith, W., Anderegg, W., Kauppi, P., Sarmiento, J., Tans, P., et al. (2017). Accelerating net terrestrial carbon uptake during the warming hiatus due to reduced respiration. *Nature Climate Change, 7*(2), 148-152. doi: 10.1038/nclimate3204.

Beer, C., Reichstein, M., Tomelleri, E., Ciais, P., Jung, M., Carvalhais, N., et al. (2010). Terrestrial Gross Carbon Dioxide Uptake: Global Distribution and Covariation with Climate. *Science, 329*(5993), 834-838. doi: 10.1126/science.1184984.

Bonan, G. B., Lombardozzi, D. L., Wieder, W. R., Oleson, K. W., Lawrence, D. M., Hoffman, F. M., & Collier, N. (2019). Model Structure and Climate Data Uncertainty in Historical Simulations of the Terrestrial Carbon Cycle (1850–2014). *Global Biogeochemical Cycles, 33*(10), 1310-1326. doi: 10.1029/2019gb006175.

Bonan, G. B., Oleson, K. W., Fisher, R. A., Lasslop, G., & Reichstein, M. (2012). Reconciling leaf physiological traits and canopy flux data: Use of the TRY and FLUXNET databases in the Community Land Model version 4. *Journal of Geophysical Research: Biogeosciences, 117*(G2), G02026. doi: 10.1029/2011jg001913.

Buermann, W., Bikash, P. R., Jung, M., Burn, D. H., & Reichstein, M. (2013). Earlier springs decrease peak summer productivity in North American boreal forests. *Environmental Research Letters, 8*(2), 024027. doi: 10.1088/1748-9326/8/2/024027.

Buermann, W., Forkel, M., O'Sullivan, M., Sitch, S., Friedlingstein, P., Haverd, V., et al. (2018). Widespread seasonal compensation effects of spring warming on northern plant productivity. *Nature, 562*(7725), 110-114. doi: 10.1038/s41586-018-0555-7.

Butterfield, Z., Buermann, W., & Keppel-Aleks, G. (2020). Satellite observations reveal seasonal redistribution of northern ecosystem productivity in response to interannual climate variability. *Remote Sensing Of Environment, 242*, 111755. doi: 10.1016/j.rse.2020.111755.

Byrne, B., Liu, J., Bloom, A. A., Bowman, K. W., Butterfield, Z., Joiner, J., et al. (2020). Outsized contribution of the semi-arid ecosystems to interannual variability in North American ecosystems. *Global Biogeochem Cycles, In Review*. doi: 10.1002/essoar.10502484.1.

Carvalhais, N., Forkel, M., Khomik, M., Bellarby, J., Jung, M., Migliavacca, M., et al. (2014). Global covariation of carbon turnover times with climate in terrestrial ecosystems. *Nature, 514*(7521), 213-217. doi: 10.1038/nature13731.

Collier, N., Hoffman, F. M., Lawrence, D. M., Keppel-Aleks, G., Koven, C. D., Riley, W. J., et al. (2018). The International Land Model Benchmarking (ILAMB) System: Design, Theory, and Implementation. *Journal of Advances in Modeling Earth Systems, 10*(11), 2731-2754. doi: 10.1029/2018ms001354.

Cox, P. M., Pearson, D., Booth, B. B., Friedlingstein, P., Huntingford, C., Jones, C. D., & Luke, C. M. (2013). Sensitivity of tropical carbon to climate change constrained by carbon dioxide variability. *Nature, 494*(7437), 341-344. doi: 10.1038/nature11882.

Danabasoglu, G., Lamarque, J.-F., Bacmeister, J., Bailey, D. A., DuVivier, A. K., Edwards, J., et al. (2020). The Community Earth System Model Version 2 (CESM2). *Journal of Advances in Modeling Earth Systems, 12*(2), e2019MS001916. doi: 10.1029/2019ms001916.

Eyring, V., Bony, S., Meehl, G. A., Senior, C. A., Stevens, B., Stouffer, R. J., & Taylor, K. E. (2016). Overview of the Coupled Model Intercomparison Project Phase 6 (CMIP6) experimental design and organization. *Geosci. Model Dev., 9*(5), 1937-1958. doi: 10.5194/gmd-9-1937-2016.

Fisher, J. B., Sitch, S., Malhi, Y., Fisher, R. A., Huntingford, C., & Tan, S. Y. (2010). Carbon cost of plant nitrogen acquisition: A mechanistic, globally applicable model of plant nitrogen uptake, retranslocation, and fixation. *Global Biogeochemical Cycles, 24*(1), GB1014. doi: 10.1029/2009GB003621.

Fisher, R. A., Wieder, W. R., Sanderson, B. M., Koven, C. D., Oleson, K. W., Xu, C., et al. (2019). Parametric Controls on Vegetation Responses to Biogeochemical Forcing in the CLM5. *Journal of Advances in Modeling Earth Systems, 11*(9), 2879-2895. doi: 10.1029/2019ms001609.

749 Friedlingstein, P., Jones, M. W., O'Sullivan, M., Andrew, R. M., Hauck, J., Peters, G. P., et al. (2019).
750 Global Carbon Budget 2019. *Earth System Science Data, 11*(4), 1783-1838. doi: 10.5194/essd-
751 11-1783-2019.
752 Friedlingstein, P., Meinshausen, M., Arora, V. K., Jones, C. D., Anav, A., Liddicoat, S. K., & Knutti, R.
753 (2014). Uncertainties in CMIP5 Climate Projections due to Carbon Cycle Feedbacks. *Journal of
754 Climate, 27*(2), 511-526. doi: 10.1175/jcli-d-12-00579.1.
755 Fu, Z., Stoy, P. C., Poulter, B., Gerken, T., Zhang, Z., Wakbulcho, G., & Niu, S. (2019). Maximum
756 carbon uptake rate dominates the interannual variability of global net ecosystem exchange.
757 *Global Change Biology, 25*(10), 3381-3394. doi: 10.1111/gcb.14731.
758 Gaubert, B., Stephens, B. B., Basu, S., Chevallier, F., Deng, F., Kort, E. A., et al. (2019). Global
759 atmospheric CO2 inverse models converging on neutral tropical land exchange, but disagreeing
760 on fossil fuel and atmospheric growth rate. *Biogeosciences, 16*(1), 117-134. doi: 10.5194/bg-16-
761 117-2019.
762 Golub, G. H., & Reinsch, C. (1971). Singular value decomposition and least squares solutions. In *Linear
763 Algebra* (pp. 134-151): Springer.
764 Hoffman, F. M., Randerson, J. T., Arora, V. K., Bao, Q., Cadule, P., Ji, D., et al. (2014). Causes and
765 implications of persistent atmospheric carbon dioxide biases in Earth System Models. *Journal of
766 Geophysical Research-Biogeosciences, 119*(2), 141-162. doi: 10.1002/2013jg002381.
767 Hu, L., Andrews, A. E., Thoning, K. W., Sweeney, C., Miller, J. B., Michalak, A. M., et al. (2019).
768 Enhanced North American carbon uptake associated with El Nino. *Sci Adv, 5*(6), eaaw0076. doi:
769 10.1126/sciadv.aaw0076.
770 Humphrey, V., Zscheischler, J., Ciais, P., Gudmundsson, L., Sitch, S., & Seneviratne, S. I. (2018).
771 Sensitivity of atmospheric CO2 growth rate to observed changes in terrestrial water storage.
772 *Nature, 560*(7720), 628-631. doi: 10.1038/s41586-018-0424-4.
773 Jung, M., Reichstein, M., Margolis, H. A., Cescatti, A., Richardson, A. D., Arain, M. A., et al. (2011).
774 Global patterns of land-atmosphere fluxes of carbon dioxide, latent heat, and sensible heat
775 derived from eddy covariance, satellite, and meteorological observations. *Journal of Geophysical
776 Research, 116*. doi: 10.1029/2010jg001566.
777 Jung, M., Reichstein, M., Schwalm, C. R., Huntingford, C., Sitch, S., Ahlström, A., et al. (2017).
778 Compensatory water effects link yearly global land CO2 sink changes to temperature. *Nature,
779 541*(7638), 516-520. doi: 10.1038/nature20780.
780 Jung, M., Schwalm, C., Migliavacca, M., Walther, S., Camps-Valls, G., Koirala, S., et al. (2020). Scaling
781 carbon fluxes from eddy covariance sites to globe: synthesis and evaluation of the FLUXCOM
782 approach. *Biogeosciences, 17*(5), 1343-1365. doi: 10.5194/bg-17-1343-2020.
783 Kannenberg, S. A., Bowling, D. R., & Anderegg, W. R. L. (2020). Hot moments in ecosystem fluxes:
784 High GPP anomalies exert outsized influence on the carbon cycle and are differentially driven by
785 moisture availability across biomes. *Environmental Research Letters, 15*(5), 054004. doi:
786 10.1088/1748-9326/ab7b97.
787 Keeling, C. D., Whorf, T. P., Wahlen, M., & van der Plichtt, J. (1995). Interannual extremes in the rate of
788 rise of atmospheric carbon dioxide since 1980. *Nature, 375*(6533), 666-670. doi:
789 10.1038/375666a0.
790 Kennedy, D., Swenson, S., Oleson, K. W., Lawrence, D. M., Fisher, R., Lola da Costa, A. C., & Gentine,
791 P. (2019). Implementing Plant Hydraulics in the Community Land Model, Version 5. *Journal of
792 Advances in Modeling Earth Systems, 11*(2), 485-513. doi: 10.1029/2018ms001500.
793 Keppel-Aleks, G., Randerson, J. T., Lindsay, K., Stephens, B. B., Keith Moore, J., Doney, S. C., et al.
794 (2013). Atmospheric Carbon Dioxide Variability in the Community Earth System Model:
795 Evaluation and Transient Dynamics during the Twentieth and Twenty-First Centuries. *Journal of
796 Climate, 26*(13), 4447-4475. doi: 10.1175/jcli-d-12-00589.1.
797 Keppel-Aleks, G., Wolf, A. S., Mu, M., Doney, S. C., Morton, D. C., Kasibhatla, P. S., et al. (2014).
798 Separating the influence of temperature, drought, and fire on interannual variability in

799   atmospheric CO2. *Global Biogeochemical Cycles, 28*(11), 1295-1310. doi:
800   10.1002/2014gb004890.
801 Köhler, P., Frankenberg, C., Magney, T. S., Guanter, L., Joiner, J., & Landgraf, J. (2018). Global
802   Retrievals of Solar-Induced Chlorophyll Fluorescence With TROPOMI: First Results and
803   Intersensor Comparison to OCO-2. *Geophysical Research Letters, 45*(19), 10,456-410,463. doi:
804   10.1029/2018gl079031.
805 Koven, C. D., Hugelius, G., Lawrence, D. M., & Wieder, W. R. (2017). Higher climatological
806   temperature sensitivity of soil carbon in cold than warm climates. *Nature Climate Change, 7*(11),
807   817-822. doi: 10.1038/nclimate3421.
808 Lasslop, G., Reichstein, M., Detto, M., Richardson, A. D., & Baldocchi, D. D. (2010). Comment on
809   Vickers et al.: Self-correlation between assimilation and respiration resulting from flux
810   partitioning of eddy-covariance CO2 fluxes. *Agricultural And Forest Meteorology, 150*(2), 312-
811   314. doi: 10.1016/j.agrformet.2009.11.003.
812 Lawrence, D. M., Fisher, R. A., Koven, C. D., Oleson, K. W., Swenson, S. C., Bonan, G., et al. (2019).
813   The Community Land Model Version 5: Description of New Features, Benchmarking, and
814   Impact of Forcing Uncertainty. *Journal of Advances in Modeling Earth Systems, 11*(12), 4245-
815   4287. doi: 10.1029/2018ms001583.
816 Lindsay, K. (2017). A Newton–Krylov solver for fast spin-up of online ocean tracers. *Ocean Modelling,*
817   *109*, 33-43. doi: 10.1016/j.ocemod.2016.12.001.
818 Lombardozzi, D. L., Lu, Y., Lawrence, P. J., Lawrence, D. M., Swenson, S., Oleson, K. W., et al. (2020).
819   Simulating Agriculture in the Community Land Model Version 5. *Journal of Geophysical*
820   *Research: Biogeosciences, 125*(8), e2019JG005529. doi: 10.1029/2019jg005529.
821 Meehl, G. A., Shields, C., Arblaster, J. M., Annamalai, H., & Neale, R. (2020). Intraseasonal, Seasonal,
822   and Interannual Characteristics of Regional Monsoon Simulations in CESM2. *Journal of*
823   *Advances in Modeling Earth Systems, 12*(6), e2019MS001962. doi: 10.1029/2019ms001962.
824 Melaas, E. K., Richardson, A. D., Friedl, M. A., Dragoni, D., Gough, C. M., Herbst, M., et al. (2013).
825   Using FLUXNET data to improve models of springtime vegetation activity onset in forest
826   ecosystems. *Agricultural And Forest Meteorology, 171-172*, 46-56. doi:
827   10.1016/j.agrformet.2012.11.018.
828 Pastorello, G., Papale, D., Chu, H., Trotta, C., Agarwal, D., Canfora, E., et al. (2017). A New Data Set to
829   Keep a Sharper Eye on Land-Air Exchanges. *EOS, 98*. doi: 10.1029/2017eo071597.
830 Piao, S., Wang, X., Wang, K., Li, X., Bastos, A., Canadell, J. G., et al. (2020). Interannual variation of
831   terrestrial carbon cycle: Issues and perspectives. *Glob Chang Biol, 26*(1), 300-318. doi:
832   10.1111/gcb.14884.
833 Poulter, B., Frank, D., Ciais, P., Myneni, R. B., Andela, N., Bi, J., et al. (2014). Contribution of semi-arid
834   ecosystems to interannual variability of the global carbon cycle. *Nature, 509*(7502), 600-603. doi:
835   10.1038/nature13376.
836 Raczka, B. M., Davis, K. J., Huntzinger, D., Neilson, R. P., Poulter, B., Richardson, A. D., et al. (2013).
837   Evaluation of continental carbon cycle simulations with North American flux tower observations.
838   *Ecological Monographs, 83*(4), 531-556. doi: 10.1890/12-0893.1.
839 Rödenbeck, C., Zaehle, S., Keeling, R., & Heimann, M. (2018a). History of El Nino impacts on the global
840   carbon cycle 1957-2017: a quantification from atmospheric CO2 data. *Philos Trans R Soc Lond B*
841   *Biol Sci, 373*(1760), 20170303. doi: 10.1098/rstb.2017.0303.
842 Rödenbeck, C., Zaehle, S., Keeling, R., & Heimann, M. (2018b). How does the terrestrial carbon
843   exchange respond to inter-annual climatic variations? A quantification based on atmospheric CO2
844   data. *Biogeosciences, 15*(8), 2481-2498. doi: 10.5194/bg-15-2481-2018.
845 Running, S. W., Nemani, R. R., Heinsch, F. A., Zhao, M., Reeves, M., & Hashimoto, H. (2004). A
846   Continuous Satellite-Derived Measure of Global Terrestrial Primary Production. *BioScience,*
847   *54*(6), 547-560. doi: 10.1641/0006-3568(2004)054[0547:Acsmog]2.0.Co;2.

848 Schwalm, C. R., Williams, C. A., Schaefer, K., Arneth, A., Bonal, D., Buchmann, N., et al. (2010).
849   Assimilation exceeds respiration sensitivity to drought: A FLUXNET synthesis. *Global Change*
850   *Biology, 16*(2), 657-670. doi: 10.1111/j.1365-2486.2009.01991.x.
851 Shi, M., Fisher, J. B., Brzostek, E. R., & Phillips, R. P. (2016). Carbon cost of plant nitrogen acquisition:
852   global carbon cycle impact from an improved plant nitrogen cycle in the Community Land
853   Model. *Global Change Biology, 22*(3), 1299-1314. doi: 10.1111/gcb.13131.
854 Tagesson, T., Schurgers, G., Horion, S., Ciais, P., Tian, F., Brandt, M., et al. (2020). Recent divergence in
855   the contributions of tropical and boreal forests to the terrestrial carbon sink. *Nature Ecology &*
856   *Evolution, 4*(2), 202-209. doi: 10.1038/s41559-019-1090-0.
857 Wang, W., Ciais, P., Nemani, R. R., Canadell, J. G., Piao, S., Sitch, S., et al. (2013). Variations in
858   atmospheric CO2 growth rates coupled with tropical temperature. *Proc Natl Acad Sci U S A,*
859   *110*(32), 13061-13066. doi: 10.1073/pnas.1219683110.
860 Wieder, W. R., Lawrence, D. M., Fisher, R. A., Bonan, G. B., Cheng, S. J., Goodale, C. L., et al. (2019).
861   Beyond Static Benchmarking: Using Experimental Manipulations to Evaluate Land Model
862   Assumptions. *Global Biogeochem Cycles, 33*(10), 1289-1309. doi: 10.1029/2018GB006141.
863 Wozniak, M. C., Bonan, G. B., Keppel-Aleks, G., & Steiner, A. L. (2020). Influence of Vertical
864   Heterogeneities in the Canopy Microenvironment on Interannual Variability of Carbon Uptake in
865   Temperate Deciduous Forests. *Journal of Geophysical Research: Biogeosciences, 125*(8),
866   e2020JG005658. doi: 10.1029/2020jg005658.
867 Zeng, N., Mariotti, A., & Wetzel, P. (2005). Terrestrial mechanisms of interannual CO2 variability.
868   *Global Biogeochemical Cycles, 19*(1). doi: 10.1029/2004gb002273.
869 Zhang, X., Gurney, K. R., Peylin, P., Chevallier, F., Law, R. M., Patra, P. K., et al. (2013). On the
870   variation of regional CO2 exchange over temperate and boreal North America. *Global*
871   *Biogeochemical Cycles, 27*(4), 991-1000. doi: 10.1002/gbc.20091.
872 Zhang, Y., Joiner, J., Gentine, P., & Zhou, S. (2018). Reduced solar-induced chlorophyll fluorescence
873   from GOME-2 during Amazon drought caused by dataset artifacts. *Global Change Biology,*
874   *24*(6), 2229-2230. doi: 10.1111/gcb.14134.
875